Mid-infrared emissivity of crystalline silicon solar cells

A. Riverola[1], A. Mellor[2], D. Alonso Alvarez[2], L. Ferre Llin[3], I. Guarracino[4], C. N. Markides[4], D. J. Paul[3], D. Chemisana[1*], N. Ekins-Daukes[2]

[1] Applied Physics Section of the Environmental Science Department, University of Lleida, 25001, Lleida, Spain

[2] Department of Physics, Imperial College London, London SW7 2AZ, UK

[3] School of Engineering, University of Glasgow, Glasgow G12 8LT, UK

[4] Clean Energy Processes (CEP) Laboratory, Department of Chemical Engineering, Imperial College London, London SW7 2AZ, UK

Abstract

The thermal emissivity of crystalline silicon photovoltaic (PV) solar cells plays a role in determining the operating temperature of a solar cell. To elucidate the physical origin of thermal emissivity, we have made an experimental measurement of the full radiative spectrum of the crystalline silicon (c-Si) solar cell, which includes both absorption in the ultraviolet to near-infrared range and emission in the mid-infrared. Using optical modelling, we have identified the origin of radiative emissivity in both encapsulated and unencapsulated solar cells. We find that both encapsulated and unencapsulated c-Si solar cells are good radiative emitters but achieve this through different effects. The emissivity of an unencapsulated c-Si solar cell is determined to be 75% in the MIR range, and is dominated by free-carrier emission in the highly doped emitter and back surface field layers; both effects are greatly augmented through the enhanced optical outcoupling arising from the front surface texture. An encapsulated glass-covered cell has an average emissivity around 90% on the MIR, and dips to 70% at 10 μm and is dominated by the emissivity of the cover glass. These findings serve to illustrate the opportunity for optimising the emissivity of c-Si based collectors, either in conventional c-Si PV modules where high emissivity and low-temperature operation is desirable, or in hybrid PV-thermal collectors where low emissivity enables a higher thermal output to be achieved.

1. Introduction

Improving the energy yield of photovoltaic (PV) solar cells is of ongoing concern. Of the many types of PV solar cell that have been developed, the crystalline silicon (c-Si) cell is by far the most commercially successful, though by no means the most efficient. This is a technology that is reaching its fundamental efficiency limits, and whose efficiency has plateaued over many years: a world record of 26.3% was announced in 2017 [1], to be compared to 24.4% in 1998 [2]. In this context, the scope for this technology to undergo significant further efficiency gains under standard test conditions (STC) is limited.

Despite their plateauing efficiency at STC, there remains an opportunity to improve the power output c-Si solar cells under real operating conditions. The efficiency of most PV cells decreases linearly with increasing temperature, the so-called temperature

coefficient of today's commercial c-Si based cells being between 0.28 - 0.52 %/°C [3]. Whereas the STC temperature is 25 °C, cells in the field typically operate closer to 50 °C [4]. Assuming a rated efficiency of 25% at STC, this implies an efficiency drop of nearly 3 percentage points.

Operating temperatures can be reduced by either passive or active cooling. Passive cooling is achieved by transmitting heat by radiation, natural convection and conduction, from the generation zone to the dissipation area [5,6], while active cooling systems transfer heat either to a tube that flows at the cell back contact [7] or the cell is directly immersed in a dielectric fluid that extracts the heat [8]. Hence, active systems consume energy to obtain higher cooling capabilities. These are all costly or bulky systems, hard to implement in large scale PV deployment without a significant increase in the cost of energy. More recently, it has been proposed that solar cells can be cooled radiatively via so-called emissivity control [9,10]. Introducing an array of silica pyramids onto the cover glass changes the emission spectrum maximising thermal emission through the atmospheric transmission window into the cold space beyond the atmosphere, while preserving the solar absorption properties [9]. This is a particularly attractive means of improving the operating efficiency due to its evolutionary nature: emissivity control measures can be added to an existing cell or module and so their fabrication does not disrupt processing chains that have already achieved economies of scale. What's more, radiative cooling is seen as an increasingly encouraging approach following the landmark achievement of passive radiative cooling of a body (not a PV cell) below ambient air temperature under direct sunlight [11].

In another application, there also exists the motivation to do the opposite and suppress the thermal emission of PV cells and modules. Specifically, in hybrid photovoltaic-thermal (PV-T) systems the thermal efficiency can be improved using spectrally-selective low-emissivity coatings to reduce radiative thermal losses [12,13]. Indium Tin Oxide (ITO) or aluminium-doped zinc oxide (AZO) films deposited by sputtering have been used as low-emissivity coatings, since they are highly reflective in the mid-infrared [14].

The radiative emissivity of PV cells is therefore gaining increasing interest in the community. However, despite being a fundamental property of the solar cell, very little is known about the emissivity of real devices and its physical origins. Sopori et al. modelled the emissivity of polished and textured silicon wafers in the $0.5 - 10$ μm range, with and without a thick (1 μm) dielectric coating as a function of doping and temperature [15,16]. However, these structures are far from real solar cells, in that they are uniformly doped and have texturing on only one side. Santbergen and van Zolingen studied numerically and experimentally the absorptivity, which is equal to the disperse emissivity via the Kirchoff relation, of PV cells up to 1.7 μm, reporting a 90% absorption of the AM1.5 spectrum in this range and the contribution of each layer of the structure [17]. Recently, the emissivity of silicon solar cells up to 25 μm was considered to be equal to the emissivity of a planar p-doped silicon wafer [9,10]. This wafer is similar to the typical base region on commercial silicon cells. However, this assumption does not consider the

impact of the texture and the highly doped regions, which are shown in the present work to dominate the emissivity of an unencapsulated c-Si solar cell.

In this paper, the emissivity of presently-manufactured silicon solar cells has been measured in the 0.35 – 16 μm range, and the first full radiative model of a solar cell considering both absorption in the spectral range of sunlight and thermal emission in the mid-infrared (MIR) has been developed. The model considers the complete cell structure with realistic layer properties and front and back textures. We demonstrate that a c-Si solar cell is highly emissive in the MIR, and that this is mostly due to the highly doped, but very thin, emitter and back-surface field layers. These highly doped layers have been overlooked in previous MIR emissivity studies, although their contribution to NIR absorption was recognised by Santbergen and van Zolingen [17].We also provide a discussion of how light trapping/outcoupling contributes to emissivity and in which spectral regions, and investigate how changes to device parameters such as doping levels and texture angle may affect the emissivity. This is important since parameter changes in future PV-cell designs may have unintended effects on the emissivity, or the cell design may be intentionally changed in order to control emissivity. The model is then used to predict the emissivity of an encapsulated PV cell under soda-lime-silica low-iron glass, from which we deduce that the MIR emissivity of a PV module is also very high and almost independent of the underlying solar cell structure. The presented study serves to underpin ongoing research into emissivity control, and to better understand a basic property of the c-Si solar cell, which is becoming one of the world's most ubiquitous optoelectronic devices.

2. Methods

Absorptivity/emissivity measurements were performed on commercially available monocrystalline c-Si solar cells, purchased from Bolisheng Technology [18], which are considered to be representative of most commercially produced aluminium-back-surface-field (Al-BSF) c-Si solar cells. The topology of the surface texture was measured with a WITec Alpha 300RS atomic force microscopy (AFM) system. This confirmed a texture of randomly sized pyramids with an elevation angle close to 55°, which is known to be typical of industrially produced c-Si solar cells [19]. An AFM micrograph is shown in Fig. 1(a), demonstrating pyramid sizes on the order of 2 μm in height. It was confirmed by the scanning electron microscopy (SEM) Leo Gemini 1525 that the aluminium back contact was deposited on top of a textured surface.

The dispersive emissivity, E, of a body is equal to its absorptivity (under thermodynamic equilibrium), A, via the Kirchhoff relation. Emissivity can therefore be measured indirectly by measuring reflectivity, R, and transmissivity, T, and invoking the relation:

$$E(\lambda) = A(\lambda) = 1 - R(\lambda) - T(\lambda) \qquad (1)$$

c-Si solar cells have a surface texture on both faces, and so the reflected and transmitted light will be diffuse. The emissivity (absorptivity) of a silicon solar cell was

therefore measured, in the range 0.35 – 16 μm, via hemispherical reflection and transmission measurements using an integrating sphere, and applying Equation (1). The measurements were carried out with a Fourier-transform spectrometer Bruker IFS 66 equipped with two integrating spheres (A PTFE coated sphere for the UV/VIS/NIR range (350 – 2400 nm) and a diffuse-gold coated sphere for the MIR (1.5 – 16 μm)). Calibrated diffusely reflecting references from the National Institute of Standards and Technology (U.S) and the National Physical Laboratory (UK) are used for baseline measurements in the UV/VIS/NIR and MIR ranges respectively. The accuracy of the reflectance data is 1% in the solar range and 2% in the IR. The transmissivity of the solar cell was measured to be zero, which is attributed to the fully metalized rear.

The measurements were carried out at room temperature. However, we consider the results to be valid over the range of reasonable operating temperatures of a PV cell, given that the overall emissivity is later shown to be dominated by the highly doped silicon regions, and that the emissivity of highly doped silicon is known to have a negligible temperature variation up to hundreds of degrees Celsius [20].

The absorptivity/emissivity of the c-Si solar cell was modelled over the full experimental range (0.35 – 16 μm) using the OPTOS formalism [21,22], which is a steady-state scattering-matrix approach that can be formulated to consider all photonic interactions with surface textures, interference coatings, and absorbing/emitting layers. Using this type of approach is of critical importance to accurately model photon absorption and emission from a textured c-Si solar cell. Any photon that is emitted somewhere inside the device can, in general, be internally reflected at any interface and make multiple passes of the solar cell, undergoing numerous reflections and transmissions at different interfaces, before either escaping into the surroundings or being reabsorbed. Equivalently, any photon incident from outside can make many passes of the cell before being absorbed or escaping. Therefore, an accurate calculation of the emissivity/absorptivity must take all these interactions into account. The OPTOS formalism performs an angular discretization within the solar cell and considers the irradiance within each angular element as elements of a vector. Matrices are then constructed to describe the attenuation/amplification of these irradiances due to absorption/emission within the different layers as well as the redistribution of these irradiances caused by scattering from the textured surfaces and reflection and transmission from interference coatings. Solution of a set of matrix equations yields the angular-resolved irradiance in each layer in the steady state from which the layer-dependent absorptivity is calculated. The emissivity is taken to be equal to the absorptivity via the Kirchoff relation. Properly formulated, this approach treats smaller features wave-optically, and larger features geometric optically, and is therefore faster and more accurate than so-called full-wave-optical calculations, which make the false assumption of infinite spatial and temporal coherence, and thus predict interference phenomena that are not observed experimentally [23]. The details of the specific implementation of OPTOS for this problem, along with the assumptions made are provided in the Appendix.
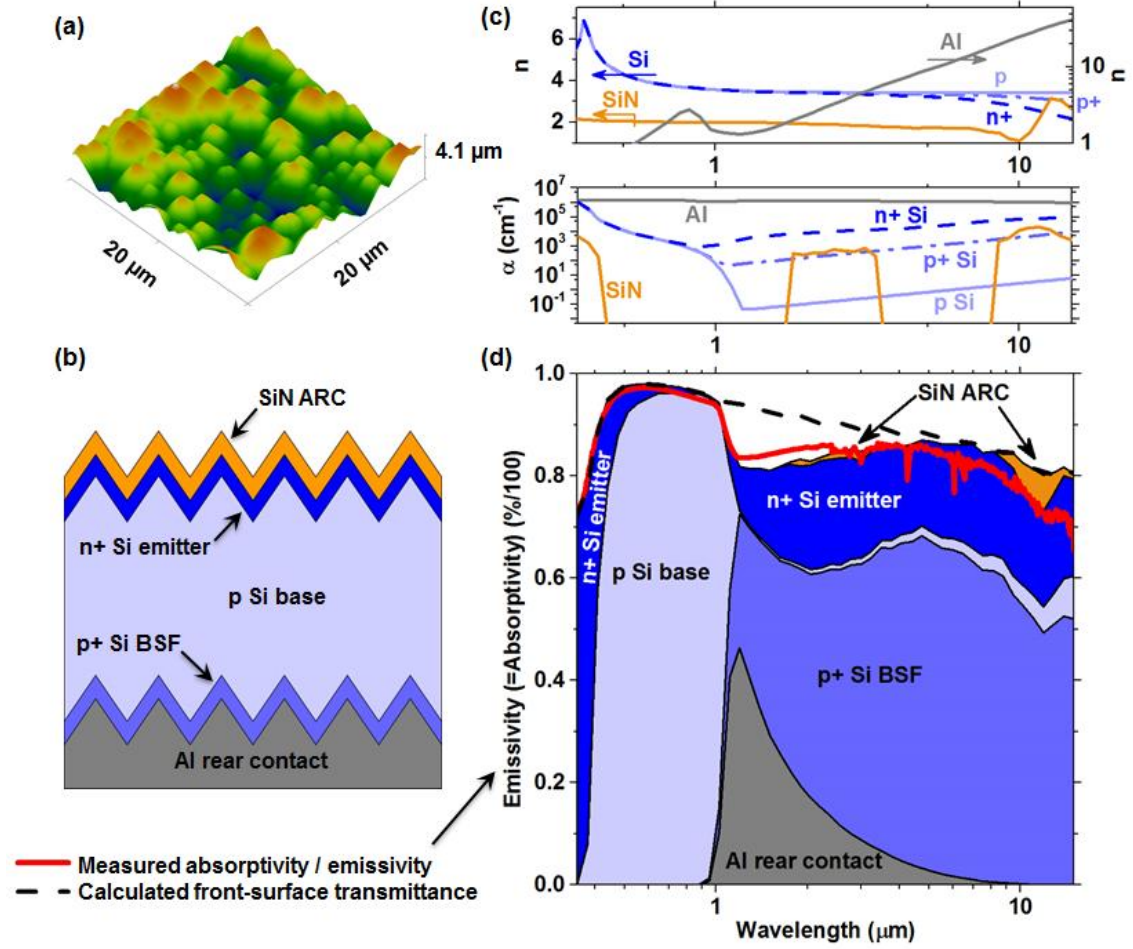
Figure 1: Model details and results together with experimental findings. (a) Atomic Force Microscopy (AFM) micrograph of the front texture of the c-Si cell under investigation. (b) Cross section schematic of the modelled solar cell structure (not drawn to scale). (c) Optical constants used in the model. (d) Measured (red line) and modelled (total filled area) emissivity/absorptivity of c-Si solar cells. The individual filled areas show the contribution of each layer to the emissivity/absorptivity.

At present, homojunction c-Si solar cells with a diffused front-side emitter, aluminium rear reflector and back surface field (BSF) formed by aluminium diffusion via annealing dominate manufacture and are well documented in the literature [24]. A cross section of the modelled solar cell structure is shown in Fig. 1(b). The cells are based on a standard low-doped p-type wafer (the base) with the above described surface texture on both sides. On the front there is a thin heavily-doped n^+ c-Si emitter layer and above this a SiN anti-reflection coating (ARC). On the rear, there is a heavily-doped p^+ c-Si BSF layer, and behind this an Al reflector, which is assumed to be optically thick. The ARC, emitter and BSF are all treated as homogeneous layers that are conformal with the surface texture. The thicknesses and doping concentration of the different layers, taken from various literature sources, are shown in Table 1. The front contact fingers are not considered explicitly in the simulations, but rather assumed to induce a non-dispersive 2% reduction of the emissivity (= absorptivity) due to shading. The finger width was measured to be 80 nm and the finger spacing 2 mm, implying a shading fraction of 4%. However, the short-wavelength range is better fit if a shading factor of 2 % is used. This could be because the

metal finger is not 100 % reflective. Since overall effect of the shading is small, a shading factor if 2 % is used and this discrepancy is not studied in further detail.

The optical constants used for all materials are shown in Fig. 1(c), represented as the real part of the refractive index, n, and the absorption coefficient, α; the latter is related to the imaginary part of the refractive index, k, via $\alpha = 4\pi k/\lambda$. The optical constants for Al are taken from Palik [25]. For c-Si, the optical constants depend on the doping level and so we take three sets of data corresponding to the emitter, base, and BSF layers. The doping dependent n for c-Si was taken from Schumann et al. [26], whereas the doping dependent α was taken from a combination of parametric models: the Baker-Finch model [27] for near band gap wavelengths ($\lambda < 1.15$ µm), the Vardanyan et al. model [28] from 1.15 µm to 6 (8) µm, for n (p) type doping, and the Schroder model [29] for longer wavelengths. SiN optical data was taken from Philipp [30] in the range 0.3 - 1.25 µm. For the MIR, no literature data was found, and so SiN films were deposited on glass substrates and measured using ellipsometry (IR-VASE system from J. A. Woollam Co. systems) yielding the plotted data in Fig. 1(c).

Table 1: Layer thicknesses and doping concentrations used in the model

Layer	Thickness	Doping (cm^{-3})	Reference
SiN ARC	74 nm	-	[17]
n+ Si emitter	55 nm	3.3×10^{20}	[17]
p Si base	145 µm	10^{16}	[17,18]
p+ Si BSF	4.3 µm	1.5×10^{19}	[31]
Al rear contact	Semi-infinite	-	[25]

3. Results

3.1 MIR emissivity of an unencapsulated c-Si solar cell

The measured emissivity/absorptivity of the unencapsulated c-Si solar cell is shown as a red line in Fig. 1(d). The solar cell is highly absorptive/emissive at all wavelengths in the 0.35 – 16 µm range. The absorption is above 90% between 400 and 1000 nm; indeed, the solar cell is engineered to absorb strongly in this range for photogeneration. The absorptivity drops slightly above 1000 nm, close to the c-Si bandgap, but remains above 80% up to 10 µm, and above 70% out to 16 µm. This range includes the 8 – 13 µm atmospheric transmission window, which also coincides with the thermal emission peak at reasonable solar cell operating temperatures. This is in contrast to the absorptivity/emissivity of a low-doped untextured Si wafer, which drops to below 20% for wavelengths above 1100 nm, corresponding to the silicon bandgap wavelength [9,10]. This discrepancy suggests that elements of the device structure other than the wafer base are responsible for the high emissivity at long wavelengths. This is investigated in the following section using the model described in Methods.

3.2 The origin of high-emissivity in c-Si solar cells

The results of the simulation are shown as the filled areas in Fig. 1(d), where the total filled area represents the total emissivity (= absorptivity). We first observe the good agreement between experiment and simulation throughout the $0.35 - 16$ μm range, which we view as a validation of the method. Above the bandgap energy ($\lambda < 1100$ nm), absorption is dominated by band-to-band absorption in the base as expected. Below the bandgap energy ($\lambda > 1100$ nm), band-to-band absorption/emission falls to zero and the absorptivity/emissivity becomes dominated by free carrier absorption/emission in the highly doped emitter and BSF, and in the Al reflector. There is also some free carrier absorption/emission in the low-doped base, but this makes a small contribution.

The total absorptivity of the solar cell is the product of the front-surface transmittance (i.e. the fraction of incident photons that are coupled into the device upon incidence) and the internal absorbance (the fraction of in-coupled photons that are absorbed)[1]. The front-surface transmittance is plotted as a black dashed curve in Fig. 1(d). In the 1 - 6 μm range, the front surface transmittance is higher than the total absorption/emission, meaning that the internal absorbance is below unity. Here, all layers are weakly absorbing and therefore light trapping due to the surface texture is playing an important role in the total absorption/emission. Conversely, in the 0.35 - 1 μm and 6 - 16 μm ranges, the front surface transmittance is exactly equal to the total absorption/emission. Here, the combined layers are strongly absorbing/emitting, and light trapping is of little or no importance to the total absorption/emission. We therefore denote the three regimes in Fig. 1(d) as transmittance limited ($0.35 - 1$ μm), not transmittance limited ($1 - 6$ μm), and again transmittance limited ($6 - 16$ μm).

It should be observed that the transition from not-transmittance-limited to transmittance-limited corresponds to a peak in the calculated emissivity at around 6 μm. In the measured data, this peak is observed at closer to 4 μm, suggesting that the transition may occur at this wavelength in the experimental sample. This discrepancy between the modelled and measured data may be due to our assumptions regarding the doping levels or regarding how the surface texture is modelled (see Appendix).

In summary, it is the omission of the highly doped regions and surface texture that have caused the emissivity of a c-Si solar cell to be understated in previous works, which assumed the emissivity to be around 25% in the MIR range [9,10]. These results show that the MIR emissivity is closer to 75%, meaning that a bare c-Si solar cell is an efficient thermal radiator. In a standard PV module, the overall emissivity is also affected by the cover glass, whose effect is described later. However, in glazed and evacuated PV-T collectors, the PV cells can be exposed directly to the vacuum beneath the glazing, and so the high emissivity of a bare PV cell implies a significant thermal loss in this type of

---

[1] Equivalently, the total emissivity is the product of the front-surface transmittance and the internal emittance, where the internal emittance is exactly equal to the internal absorbance.

collector. There is therefore significant scope for radiative emissivity suppression in PV-T collectors [12,13].

3.3 Effect of the solar cell parameters or structure on the MIR emissivity

As described in the introduction, the use of photonic structures for emissivity control has gained recent success in general radiative cooling [11] and may be a promising mean of cooling PV solar cells [9]. However, it is also interesting to see how sensitive the emissivity is to device parameters such as doping densities or surface texture, to infer how changing device architecture may affect emissivity. The sensitivity analysis is shown in Fig. 2. Fig. 2 (a)-(c) show the sensitivities of the emissivity spectra to changes in emitter and BSF doping and the texture steepness respectively. Fig. 2 (d) summarizes the results for a single wavelength of 9 μm, which is particularly relevant to radiative cooling since it is close to the black body emission peak and within the atmospheric transparency window.
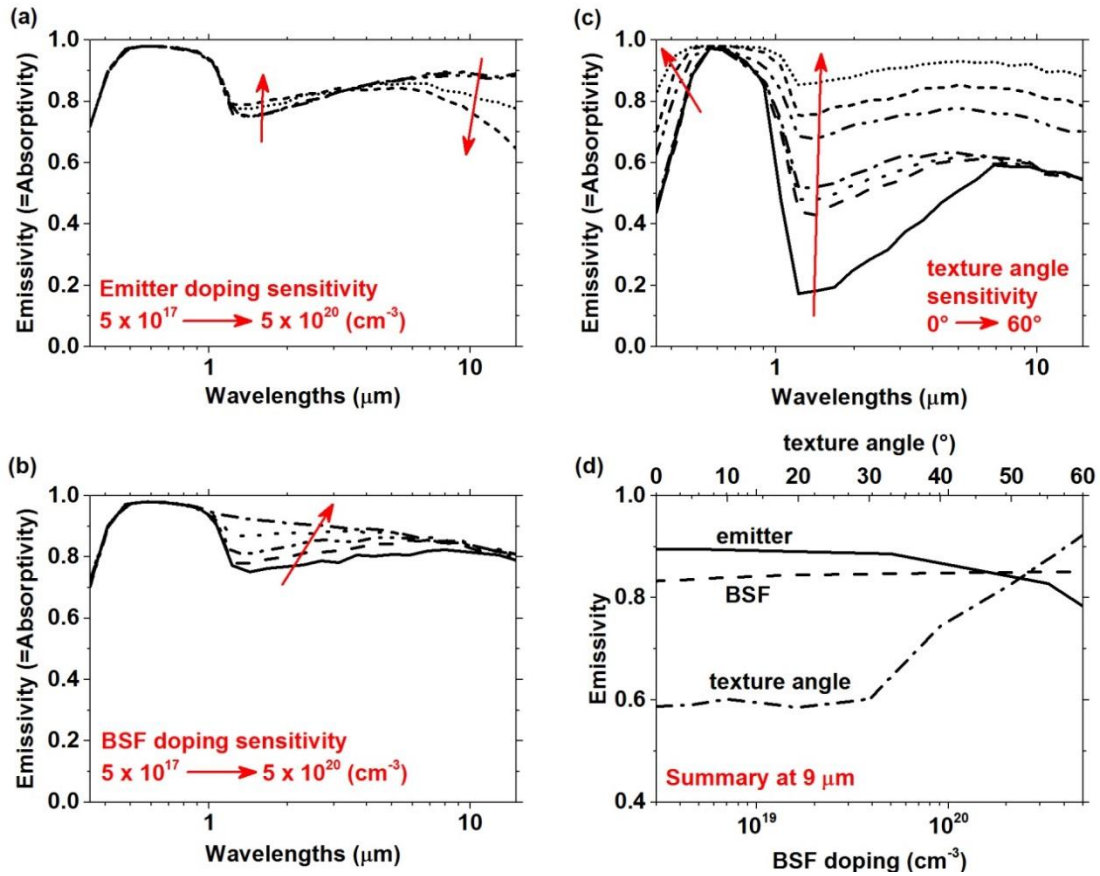

Figure 2: Dependence of the emissivity on the solar cell parameters. (a) Dependence on the emitter doping. (b) Dependence on the BSF doping. (c) Dependence on the texture steepness of both front and rear surfaces. (d) Detail of the emissivity dependence on the corresponding parameters at 9 μm.

The emitter doping (Fig. 2(a)) has an impact in the MIR emissivity and near infrared (NIR) absorptivity. Increasing the doping level marginally enhances the NIR absorptivity due to the increased free-carrier concentration. However, the effect is the

opposite in the MIR, where an increased doping level leads to a reduced emissivity. This is due to the plasma frequency being pushed towards shorter wavelengths making the emitter more reflective in the MIR [32]. At 9 μm, the emissivity starts to fall for doping concentrations above 5×10^{19} cm^{-3} (see Fig. 2(d)).

The effect of the BSF doping (Fig. 2(b)) is limited to the previously discussed *not-transmittance-limited* regime (1 – 6 μm). An increased doping level increases the NIR absorptance/emittance of the BSF layer. At the highest doping level, the overall absorptivity/emissivity becomes limited by the front-surface transmittance. Finally, Fig. 2(d) shows that the effect on the emissivity at 9 μm is negligible.

Texture steepness (Fig. 2(c)) has been found to be a key factor. Steps of 10º from 0º to 60º have been considered. The transmittance of the front surface and the light-trapping are enhanced when increasing the texture angle. As a result, reducing the texture angle reduces the emissivity at 9 μm, reaching a minimum of 60% at 30º and then levelling off. This is in accordance with previous results suggesting that the absorption remains low up to 25º [17], albeit at lower wavelengths than those studied here. Nonetheless, the texture steepness is largely determined by the c-Si structure and it is not easy to vary in practice.

In summary, the only parameter change that significantly increases the MIR emissivity is an increase in the texture angle. Conversely, the MIR emissivity can be significantly reduced either by employing planar cells or those with low texture angles, or significantly increasing the emitter doping level.

3.4 Effect of encapsulation on the emissivity

In a PV module, c-Si solar cells are encapsulated in ethylene vinyl acetate (EVA) and then covered with around 3 mm of soda-lime-silica low-iron glass [17,33]. This serves to protect the solar cells from dust and moisture and provide rigidity. The emissivity of an encapsulated c-Si solar cell with glass cover has been calculated using the above simulation method. The EVA optical properties are considered to be akin to the glass and therefore both layers were modelled together [17]. This is justified since EVA and soda-lime-silica exhibit a similar real part of the refractive index in the VIS-NIR and MIR leading to an almost ideal optical coupling, they diverge however in the ultraviolet region where the EVA is highly absorptive [34].

Fig. 3 shows that for wavelengths shorter than 1100 nm (above the bandgap energy), the absorptivity/emissivity is flatter than in the unencapsulated case but equally dominated by band-to-band absorption in the bulk since the cover glass absorptivity in this range is weak. In the NIR, again the Al rear contact is the principle absorber and a reduced fraction of photons, initially transmitted into the cell, escape the front texture. The out-coupling effect is greater than in the previous case due to the higher transmittance of the air-glass interface. The main effect of encapsulation on the emissivity comes in the MIR region ($\lambda > 5$ μm), where the cover glass absorbs all the incident photons achieving an emissivity around 90%. There is an emissivity dip at around 9 μm due to a polariton

resonance [32]. Previous studies, which have assumed the cover glass to be composed of pure silica, have shown this dip to be broader and deeper, reaching a minimum of 25%. Using optical data for the soda-lime-silica low-iron glass typically employed in PV modules indicates a minimum closer to 75%, indicating that an encapsulated and glass-covered c-Si solar cell remains an efficient radiative emitter.
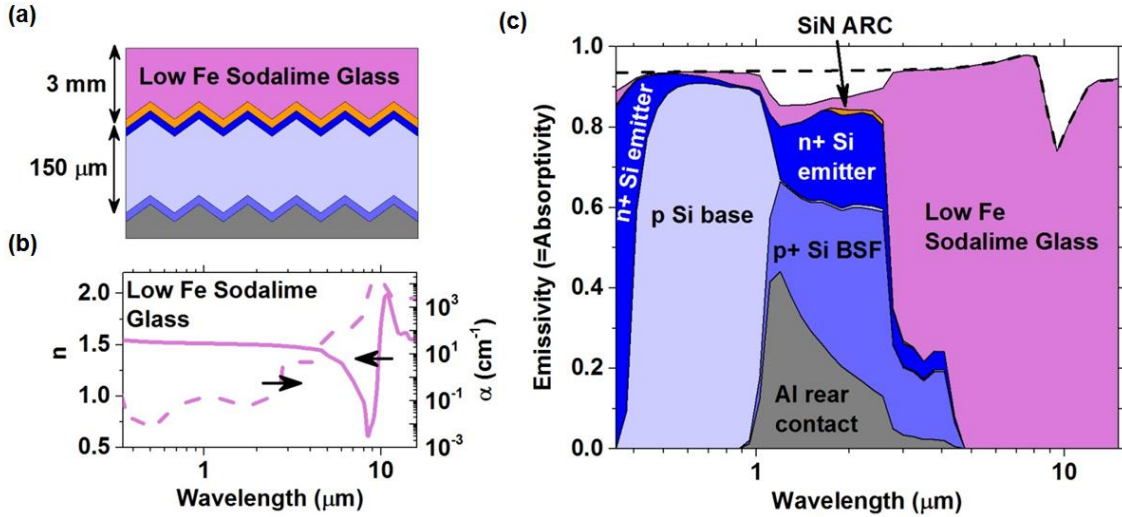

Figure 3: Emissivity of an encapsulated c-Si solar cell. (a) Cross section schematic of the modelled encapsulated solar cell structure (not drawn to scale). (b) Optical constants used in the model. (c) Modelled (total filled area) emissivity/absorptivity of encapsulated c-Si solar cells. The individual filled areas show the contribution of each layer to the emissivity/absorptivity.

4. Conclusions

The emissivity of commercial silicon solar cells has been experimentally measured and modelled into the full radiative spectrum, which includes the sunlight spectrum range and the thermal emission in the mid-infrared (MIR). In addition, the model encloses the complete cell structure and texture. Both unencapsulated and encapsulated c-Si solar cells are found to be good radiative thermal emitters. The mid-infrared emissivity of the unencapsulated case is around 80%, dominated by highly doped regions and enhanced by the presence of the surface texture. The MIR emissivity of the encapsulated cell is around 90% due to the high emissivity of the cover glass. The emissivity dips to 75% at 9 μm, though this dip is not as pronounced as suggested in some previous works that assume pure silica instead of low-iron soda-lime-silica. Furthermore, a sensitivity analysis on the main cell parameters shows that the texture steepness is a major factor which can vary the NIR and MIR emissivity from around 25% to 85% and from 60% to 90%, respectively. Assuming that modern silicon solar cells are mainly textured with elevation angles around 55º, we can conclude that the mid-infrared emissivity of commercial silicon solar cells will be high (>= 75%) if there is at least one highly doped layer.

The results were obtained using the first full radiative model including UV/VIS/NIR absorption and MIR emission and validated against experimental data. Our results show the scope that exists for emissivity control. While there is some scope for increasing solar cell efficiency by enhancing radiative emission, our results show that most PV modules in the field are already good radiative thermal emitters. Conversely, it is likely that the thermal efficiency of PV-T collectors is significantly limited by radiative losses. Suppressing these by employing measures to reduce MIR emissivity is expected to lead to improved thermal performance of PV-T collectors. The above results confirm that the emissivity of commercial silicon solar cells has been understated in recent works. For energies below the bandgap, the thick base layer of the solar cell plays no role in determining the emissivity but rather the much thinner layers, confirming that the complete structure, layers and texture, needs to be considered and properly modelled. The light trapping effect together with the free carrier absorption at the highly doped emitter and BSF layer and the absorption at the back contact are found to be crucial considerations.

This work has focused on the so-called (Al-BSF) solar cell, this being the dominant Technology in present production. However, PERC and heterojunction solar cells are expected to gain market share in the near future [24]. The emissivity of these different architectures should be studied in future work.

Acknowledgements

References

[1]   K. Yoshikawa, H. Kawasaki, W. Yoshida, T. Irie, K. Konishi, K. Nakano, T. Uto, D. Adachi, M. Kanematsu, H. Uzu, K. Yamamoto, Silicon heterojunction solar cell with interdigitated back contacts for a photoconversion efficiency over 26%, Nat. Energy. 2 (2017) 17032. doi:10.1038/nenergy.2017.32.

[2]   J. Zhao, A. Wang, M.A. Green, F. Ferrazza, 19.8% Efficient "Honeycomb" Textured Multicrystalline and 24.4% Monocrystalline Silicon Solar Cells, Appl. Phys. Lett. 73 (1998) 1991–1993. doi:10.1063/1.122345.

[3]   B. Marion, Comparison of predictive models for photovoltaic module performance, in: 2008 33rd IEEE Photovolatic Spec. Conf., IEEE, 2008: pp. 1–6. doi:10.1109/PVSC.2008.4922586.

[4]   M. Koehl, M. Heck, S. Wiesmeier, J. Wirth, Modeling of the nominal operating cell temperature based on outdoor weathering, Sol. Energy Mater. Sol. Cells. 95 (2011) 1638–1646. doi:10.1016/j.solmat.2011.01.020.

[5]   K. Araki, H. Uozumi, M. Yamaguchi, A simple passive cooling structure and its heat analysis for 500 X concentrator PV module, Conf. Rec. Twenty-Ninth IEEE Photovolt. Spec. Conf. 2002. (2002) 2–5. doi:10.1109/PVSC.2002.1190913.

[6]   S. Fork, David, Horne, Passively Cooled Solar Concentrating Photovoltaic Device, US Patent US2007/0256724 A1, 2006.

[7]   J.S. Coventry, Performance of a concentrating photovoltaic/thermal solar collector, Sol. Energy. 78 (2005) 211–222. doi:10.1016/j.solener.2004.03.014.

[8]   L. Liu, L. Zhu, Y. Wang, Q. Huang, Y. Sun, Z. Yin, Heat dissipation performance of silicon solar cells by direct dielectric liquid immersion under intensified illuminations, Sol. Energy. 85 (2011) 922–930. doi:10.1016/j.solener.2011.02.007.

[9]   L. Zhu, A. Raman, K.X. Wang, M.A. Anoma, S. Fan, Radiative cooling of solar cells, Optica. 1 (2014) 32–38. doi:10.1364/OPTICA.1.000032.

[10]   L. Zhu, A.P. Raman, S. Fan, Radiative cooling of solar absorbers using a visibly transparent photonic crystal thermal blackbody., Proc. Natl. Acad. Sci. U. S. A. 112 (2015) 12282–12287. doi:10.1073/pnas.1509453112.

[11]   A.P. Raman, M.A. Anoma, L. Zhu, E. Rephaeli, S. Fan, Passive radiative cooling below ambient air temperature under direct sunlight., Nature. 515 (2014) 540–4. doi:10.1038/nature13883.

[12]   I. Guarracino, A. Mellor, N.J. Ekins-Daukes, C.N. Markides, Dynamic coupled thermal-and-electrical modelling of sheet-and-tube hybrid photovoltaic/thermal (PVT) collectors, Appl. Therm. Eng. 101 (2016) 778–795. doi:10.1016/j.applthermaleng.2016.02.056.

[13]   A. Mellor, I. Guarracino, L.F. Llin, D. Alonso-Alvarez, A. Riverola, S. Thoms, D.J. Paul, C.N. Markides, D. Chemisana, S. Maier, N.E.- Daukes, Specially designed solar cells for hybrid photovoltaic-thermal generators, in: 2016 IEEE 43rd Photovolt. Spec. Conf., IEEE, 2016: pp. 2960–2963. doi:10.1109/PVSC.2016.7750203.

[14]   D. Alonso-Alvarez, L. Ferre Llin, A. Mellor, D.J. Paul, N.J. Ekins-Daukes, ITO and AZO films for low emissivity coatings in hybrid photovoltaic-thermal applications, Sol. Energy. 155 (2017) 82–92.

[15]   B.L. Sopori, W. Chen, S. Abedrabbo, N.M. Ravindra, Modeling emissivity of rough and textured silicon wafers, J. Electron. Mater. 27 (1998) 1341–1346. doi:10.1007/s11664-998-0094-3.

[16]   B. Sopori, W. Chen, J. Madjdpour, N.M. Ravindra, Calculation of emissivity of Si wafers, J. Electron. Mater. 28 (1999) 1385–1389. doi:10.1007/s11664-999-

0126-7.

[17] R. Santbergen, R.C. van Zolingen, The absorption factor of crystalline silicon PV cells : A numerical and experimental study, Sol. Energy Mater. Sol. Cells. 92(4) (2008) 432–444. doi:10.1016/j.solmat.2007.10.005.

[18] B. Technology, Silicon solar cellsMONO(φ165)S5LV03 125mm, (n.d.). http://www.bolisheng.com/en/product_show.asp?id=364 (accessed August 1, 2016).

[19] A. Luque, S. Hegedus, Handbook of photovoltaic science and engineering, Wiley, 2011.

[20] N.M. Ravindra, B. Sopori, O.H. Gokce, S.X. Cheng, A. Shenoy, L. Jin, S. Abedrabbo, W. Chen, Y. Zhang, Emissivity Measurements and Modeling of Silicon-Related Materials: An Overview, Int. J. Thermophys. 22 (2001) 1593–1611. doi:10.1023/A:1012869710173.

[21] J. Eisenlohr, N. Tucher, O. Höhn, H. Hauser, M. Peters, P. Kiefel, J.C. Goldschmidt, B. Bläsi, Matrix formalism for light propagation and absorption in thick textured optical sheets., Opt. Express. 23 (2015) A502-18. doi:10.1364/OE.23.00A502.

[22] N. Tucher, J. Eisenlohr, P. Kiefel, O. Höhn, H. Hauser, M. Peters, C. Müller, J.C. Goldschmidt, B. Bläsi, 3D optical simulation formalism OPTOS for textured silicon solar cells., Opt. Express. 23 (2015) A1720-34. doi:10.1364/OE.23.0A1720.

[23] M. Born, E. Wolf, Principles of optics : electromagnetic theory of propagation, interference and diffraction of light, Cambridge University Press, 1999.

[24] International Technology Roadmap for Photovoltaic (ITRPV, 2017), 2017. http://www.itrpv.net/Reports/Downloads/.

[25] E.D. Palik, Handbook of optical constants of solids, Academic Press, 1998.

[26] P. a. Schumann, W. a. Keenan, a. H. Tong, H.H. Gegenwarth, C.P. Schneider, Silicon Optical Constants in the Infrared, J. Electrochem. Soc. 118 (1971) 145. doi:10.1149/1.2407931.

[27] S.C. Baker-Finch, K.R. McIntosh, D. Yan, K.C. Fong, T.C. Kho, Near-infrared free carrier absorption in heavily doped silicon, J. Appl. Phys. 116 (2014). doi:10.1063/1.4893176.

[28] R.R. Vardanyan, V.K. Dallakyan, U. Kerst, C. Boit, Modeling free carrier absorption in silicon, J. Contemp. Phys. (Armenian Acad. Sci. 47 (2012) 73–79. doi:10.3103/S1068337212020053.

[29] D.K. Schroder, R.N. Thomas, J.C. Swartz, Free carrier absorption in silicon, IEEE Trans. Electron Devices. 25 (1978) 254–261.

[30] H.R. Philipp, Optical Properties of Silicon Nitride, J. Electrochem. Soc. 120 (1973) 295. doi:10.1149/1.2403440.

[31] T. Fellmeth, S. MacK, J. Bartsch, D. Erath, U. Jäger, R. Preu, F. Clement, D. Biro, 20.1% Efficient Silicon Solar Cell With Aluminum Back Surface Field, IEEE Electron Device Lett. 32 (2011) 1101–1103. doi:10.1109/LED.2011.2157656.

[32] M. Fox, Optical properties of solids, Oxford University Press, 2001.

[33] C.R. Kurkjian, W.R. Prindle, Perspectives on the History of Glass Composition, J. Am. Ceram. Soc. 81 (2005) 795–813. doi:10.1111/j.1151-2916.1998.tb02415.x.

[34] K.R. Mcintosh, J.N. Cotsell, J.S. Cumpston, A.W. Norris, N.E. Powell, B.M. Ketola, An optical comparison of silicone and EVA encapsulants for conventional silicon PV modules : a ray-tracing study, in: 34th IEEE Photovolt.

Spec. Conf., 2009: pp. 544–549.

[35] K. Tang, R.A. Dimenna, R.O. Buckius, Regions of validity of the geometric optics approximation for angular scattering from very rough surfaces, Int. J. Heat Mass Transf. 40 (1996) 49–59. doi:10.1016/S0017-9310(96)00073-7.

[36] J. Krč, M. Zeman, O. Kluth, F. Smole, M. Topič, Effect of surface roughness of ZnO:Al films on light scattering in hydrogenated amorphous silicon solar cells, Thin Solid Films. 426 (2003) 296–304. doi:10.1016/S0040-6090(03)00006-3.

[37] J. Krč, F. Smole, M. Topič, Potential of Light Trapping in Microcrystalline Silicon Solar Cells with Textured Substrates, Prog. Photovoltaics Res. Appl. 11 (2003) 429–436. doi:10.1002/pip.506.

[38] M. Zeman, O. Isabella, S. Solntsev, K. Jäger, Modelling of thin-film silicon solar cells, Sol. Energy Mater. Sol. Cells. 119 (2013) 94–111. doi:10.1016/j.solmat.2013.05.037.

[39] P. Kowalczewski, M. Liscidini, L.C. Andreani, Light trapping in thin-film solar cells with randomly rough and hybrid textures., Opt. Express. (2013). doi:10.1364/OE.21.00A808.

[40] J.M. Rodríguez, I. Tobias, A. Luque, Random pyramidal texture modelling, Sol. Energy Mater. Sol. Cells. 45 (1997) 241–253.

[41] Y. Yang, R.O. Buckiust, Surface Length Scale Contributions to the Directional and Hemispherical Emissivity and Reflectivity, J. Thermophys. Heat Trasnfer. 9 (1995) 653–659. doi:10.2514/3.720.

Appendix A – OPTOS implementation and model assumptions

Within the OPTOS formalism, angular space is discretised into *n* angular elements and a number of $n \times n$ matrices are constructed to describe light scattering at surfaces and propagation through homogeneous regions; the former are described by so-called redistribution matrices and the latter by the propagation matrix. The elements of the matrices must be calculated using whatever optical methods are most appropriate to the device or structure under investigation, and in general different models and assumptions can be used in different regions of the device. The OPTOS formalism is therefore a modelling framework into which other optical models are nested.

In this work, the silicon solar cell is treated using redistribution matrices B and C to describe the scattered reflection and transmission of the front and rear surfaces, and a single propagation matrix D to describe the bulk. This is depicted in Fig. A1. The OPTOS formalism for *combining* matrices B, C and D to calculate reflection and absorption can be found in Refs. [21,22], along with a validation of the general OPTOS method. Here, we describe how the matrices have been *constructed* in this work to model the absorptivity/emissivity of a textured silicon solar cell. We make the assumption that the problem can be treated in two dimensions, so that only the polar angle must be taken into account. This requires an escape factor to be incorporated into OPTOS, and is described and justified in Section A5.
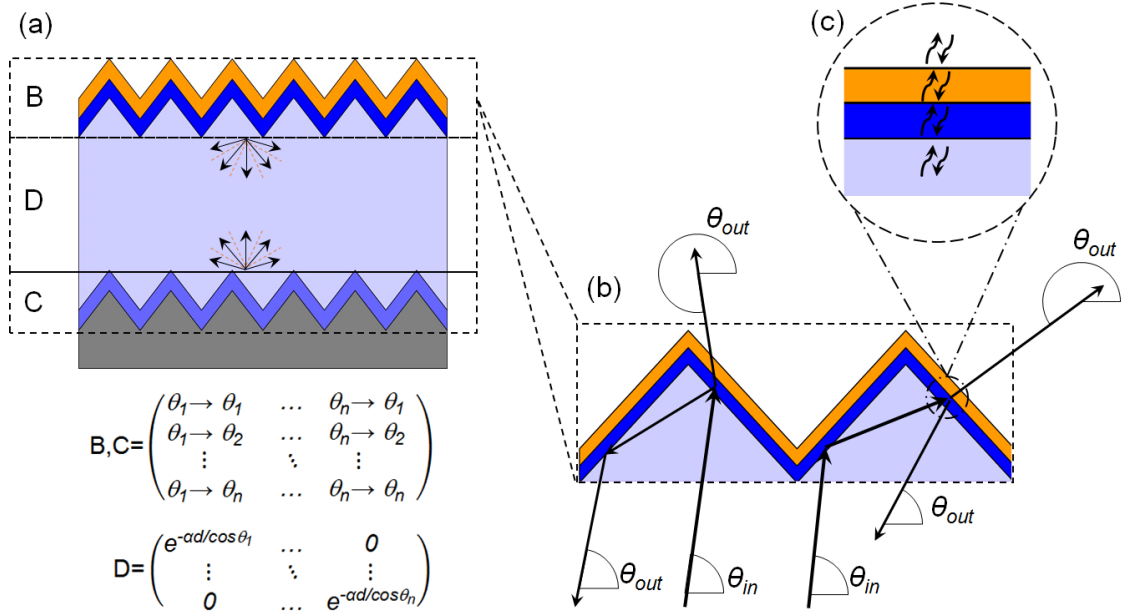

Figure. A1: OPTOS implementation. (a) The solar cell is divided into three regions, which are described by three different matrices. Propagation matrix D is a diagonal matrix constructed using the Lambert Beer law. Redistribution matrices B and C must be calculated using a combination of ray tracing and TMM applied to the textured front and rear surfaces. (b) Illustration of how ray –tracing is applied to the front surface. For each incidence angle in the angular discretization, many rays are traced with different spatial starting points. At each interaction with an interface, the probability of

15

transmission or reflection is calculated using the transfer matrix method (TMM). The exit angles of the different rays are recorded in a histogram, which forms one column of matrix B. (c) Illustration of TMM applied to the surface of a pyramid plane with emitter and ARC layer.

A1 Calculation of the redistribution matrices B and C

The redistribution matrices for the front and rear textures (B and C in Fig. A1(a)) describe how light incident on the texture at a given angle is scattered into all other angles. The structure of these matrices is depicted in Fig. A1(a); where each column specifies the redistribution of power from each incidence-angle manifold in the discretization to each other manifold. The matrices must take into account light incidence from above and below the texture and both reflected and transmitted scattering in each case. Matrix elements corresponding to incidence from within the rear reflector are set to zero.

In the solar cell under study, both front and rear textures consist of square based pyramids with an elevation angle of 55º, which are randomly sized and distributed with and an average height of 2 μm (around 4.1 μm for the larger pyramids) (Fig. 1(a)). Importantly, the pyramids are much larger than the thickness of the SiN ARC (74 nm) and the n+ emitter (55 nm) layers. We make the assumption that the light-scattering effect of the pyramids can be calculated using the geometric optics approximation, whereas reflection and transmission from the interfaces of the pyramids must be calculated in the wave optics regime due to the presence of very thin layers such as the SiN ARC (Fig. A1(b)-(c)). In practise, this is achieved by combining a Monte-Carlo ray-tracing algorithm with a transfer matrix method (TMM) to properly calculate the reflection and transmission at the pyramid planes. We also assume that the random pyramids can be effectively modelled as an array of identical triangles with 55º elevation. The geometric optics approximation renders the pyramids dimensionless and so the height and width of the pyramids does not need to be specified, just the elevation angle. These assumptions are justified in Section A5.

For a given incidence angle, a number of rays are traced with starting points chosen randomly from a spatially uniform distribution. At each interaction between a ray and a pyramid plane, the chances of being transmitted, reflected or absorbed are calculated by the TMM. The TMM assumes the pyramid plane on the front texture to be planar over an area significantly larger than the thickness of the emitter and ARC layers (see Fig. A1(c)), which is reasonable given their respective dimensions. For a ray impacting the back texture (BSF + rear contact) from within the cell, we calculate the absorptivity and the reflectivity (transmissivity = 0) at the aluminium layer by the TMM and the absorptivity at the BSF layer, either entering the texture or after being reflected at the aluminium interface, by the Lambert-Beer law. The ray's propagation is then selected randomly from the probability distribution until the ray escapes the texture, either into

the cell, air or aluminium, storing the initial and exit angular elements. If the ray is absorbed, no exit angle is recorded.

Using a Monte-Carlo approach, the previous process runs iteratively until the scattering and absorption of each angular element converges. The column sum of the redistribution matrices is normalized to the total number of traced rays for the corresponding incidence angle. This ensures conservation of power, but also implicitly records the absorption events since these cause the column sum to be less than 1.

A2 Propagation matrix D

The propagation matrix accounts for the absorption of the base region, which is optically thick and homogeneous (D in Fig. A1(a)). The intensity decreases exponentially according to Lambert-Beer's law for absorbing media and the rays' trajectory is unaltered. Therefore, the propagation matrix is diagonal and each element corresponds to the exponential function of the respective channel according to Lambert-Beer's law (see detail of matrix D in Fig. A1(a)).

A3 Calculation of the total absorption and the different contributions to the absorption

The formalism for combining the matrices, and calculating the total absorption, reflection and transmission is described in the OPTOS references [21,22]. OPTOS is configured to calculate the total absorption in the three different regions of the structure depicted in Fig. A1(a).

In this work, we have amended the formalism to further decompose the absorption into the different layers of the solar cell (emitter, ARC, base, BSF, rear reflector). This is done differently depending on the region in question. Firstly, we split the total absorptivity of the front texture (A_B) into the absorptivity at the ARC (A_{ARC}) and at the emitter ($A_{emitter}$) using the following equations, where t represents the relevant thickness:

$$A_{ARC}(\lambda) = A_B(\lambda) \frac{\alpha_{ARC}(\lambda)\, t_{ARC}}{\alpha_{ARC}(\lambda)\, t_{ARC} + \alpha_{Emitter}(\lambda)\, t_{Emitter}} \qquad (A1)$$

$$A_{Emitter}(\lambda) = A_B(\lambda) - A_{ARC}(\lambda) \qquad (A2)$$

For all silicon layers, the free carrier (A_{fc}) and band-to-band (A_{b-b}) absorption are separated from the layer total absorption (A) by the next equations where α_T is the layer total absorption coefficient and α_i is the absorption coefficient of intrinsic silicon.

$$A_{fc}(\lambda) = A(\lambda) \frac{\alpha_T(\lambda) - \alpha_i(\lambda)}{\alpha_T(\lambda)} \qquad (A3)$$

$$A_{b-b}(\lambda) = A(\lambda) - A_{fc}(\lambda) \qquad (A4)$$

Last, the absorptivities at the rear reflector (A_R) and at the BSF (A_{BSF}) are directly extracted from the model. Rays transmitted into the rear reflector get absorbed there and the absorption at the back interface corresponds with the BSF absorption.

A4 The encapsulated solar cell

The cover glass located atop of the cell, adds a new optically thick and homogeneous layer which can be treated by a new propagation matrix (D-glass). Since rays can be trapped either in the glass or in the cell, a new redistribution matrix needs to be introduced to describe the air-glass interface (B-glass). This matrix is diagonal and describes the specular reflectivity of this planar interface.

A5 Validity of modelling assumptions

We describe in the following the principle assumptions made in the modelling and discuss their validity by comparison to works in the literature. However, the primary validation of the modelling approach is the excellent agreement between experiment and calculation throughout the studied wavelength range:

1. The solar cell has been modelled in two dimensions as opposed to three dimensions. Previous studies have found 2D modelling to be sufficient for this type of structure. Santbergen and Van Zolingen studied optical absorption in a solar cell with three dimensional front and back textures obtained by an acid texture etch. They found that the absorption spectra of a number of devices could be well reproduced by modelling the texture in two dimensions and using a so-called escape factor to account for the fact that the loss cone occupies less of the total hemisphere in three dimensions than in two. In this work, we have incorporated an escape factor of 0.3 into the OPTOS formalism, which is justified by Santbergen and Van Zolingen [17].

2. Photon scattering from the surface texture has been calculated using a geometric optics method throughout the studied range (0.35 – 16 μm). Geometric optics is an approximation to more general wave optics, which becomes increasingly accurate when the feature dimensions are large compared to wavelength of the interacting light. We offer in the following a discussion of the accuracy of this approximation based on the validity study of Tang et. al [35].

   Tang et al. performed a study of the validity regime of geometric optics for angular scattering in random rough surfaces, similar to the surface textures studied here. The validity regime was determined by computing the so-called bi-directional reflection function for a range of random textures, using both geometrical optical and wave optical methods, and comparing results. The parameters determining the validity were found to be σ, τ, θ and λ. Where σ refers to the surface height root mean square (rms), τ is the surface correlation length, θ is the incident angle and λ the wavelength. Two criteria were established for determining validity. The first, stronger and rather restrictive criterion was that the angular dependence of the bi-directional reflection

function be similar between both methods over the full sphere. Regions of the parameter space fulfilling this criterion were denoted the Geometric Optics Approximation Region. The green filled area in Fig. A2 shows this validity region as a function of the surface slope (σ/τ) and $\sigma\cos(\theta)/\lambda$. The second, weaker criterion was that the specular reflection, Rs, be similar between the two methods, where the specular reflection is defined as the reflected power integrated over a wavelength range spanning 10 degrees either side of the specular reflection angle. This was denoted the Specular Approximation Region and is plotted as the blue filled area in Fig. A2.

The horizontal line in Fig. A2 shows a plot of (σ/τ) against $\sigma\cos(\theta)/\lambda$ for the 0.35 – 16 µm wavelength range studied in this work and assuming normal incidence. The used parameters of $\sigma = 0.70$ µm and $\tau = 1.8$ µm have been taken from the AFM measurement presented in Fig. 1(a). The line has been divided into the two regimes discussed in the Results section. These are Regime 1 (black lines) - transmittance-limited - below 1 µm and above 6 µm, and Regime 2 (red lines) – not-transmittance-limited – from 1µm to 6µm. It can be seen that calculations performed in Regime 2 fall within the Geometric Optics Region below 4 µm, within the Specular Region below 5.5 µm, and in neither region between 5.5 and 6 µm. Calculations performed in Regime 1 fall within the Geometric Optics Region below 1 um, and in neither region above 6 µm.

In Regime 1 - the transmittance limited regime-, the total absorption/emission is simply 1-R where R is the hemispherically integrated front surface reflectance. Therefore, the absorption in this regime is not sensitive to the angular distribution of the reflection, just its total value. As a consequence, it is not required to satisfy either criterion of Tang et al., but instead the much weaker criterion that the total reflection is accurate. In this regime, no proof is offered that the geometric optics result approximates an equivalent wave-optics result; we instead rely on the agreement between experiment and simulation shown in Fig. 1(d) for validation, and observe that, due to the weaker validity requirement, the validity considerations discussed in Tang et. al. are not explicitly contravened.

In Regime 2 - the not-transmittance-limited regime -, the validity criterion to be satisfied is stronger than in Regime 1. Here, the absorption is sensitive not only to the overall reflectance of the textures, but also on their light-trapping properties, and so the angular dependence bi-directional reflection function is expected to play a role. Up to 4 µm, all calculations lie within the Geometric Optics Region, meaning that the ray tracing algorithm should accurately predict the angular dependence of the bi-directional reflection function, and so the overall calculations should certainly be accurate in this region. From 4 – 5.5 µm, the calculations fall in the Specular Region. Here, the calculations will accurately calculate the degree of specular reflection and transmission, and therefore the so-called haze factors in reflection and transmission, if not the

exact form of the bi-directional reflection function. Other works on textured solar cells have found the haze factor to be a principle measure of the light trapping properties of a surface texture [36–39], which explains the good agreement between experiment and calculation in this range in Fig. 1(d). Above 5.5 μm, the calculations lie outside both regions, meaning that neither the angular dependence nor the haze factor will be accurately calculated. However, these calculations lie in Regime 1 of our study. As discussed above, the absorption in Regime 1 depends only on the total reflectance and transmittance of the front texture, not on its angular distribution or haze factor. This explains why good agreement is maintained in this range.
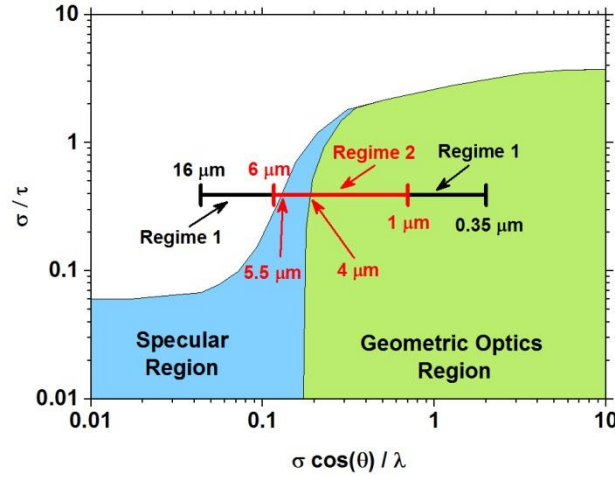

Figure. A2: Validity regime for geometric-optics.

3. The texture has been modelled as a regular array, not random. Rodríguez et al. studied the reflectivity of random and periodic textures of typical solar cells in order to evaluate whether it is important to consider the complete random texture for ray-tracing algorithms or not. Their results showed that regular and random textures result in a similar angular reflectivity for a wide range of incidence angles and therefore a complete random pyramidal texture modelling is not necessary [40]. Yang and Buckius demonstrated that the radiative properties of random surfaces are dominated by the ratio between the surface height and transverse length (called surface slope), suggesting that different textures with similar surface slopes exhibit similar hemispherical emissivity. Only minor variations in directional emissivity were reported between random and symmetrical configured surfaces [41]. It should be observed that we are only able to make this assumption in the geometric optics regime: assuming periodicity in a full-wave optical calculation would create artificial interference effects such as Rayleigh anomalies, which would significantly reduce the accuracy of the model.